The Effective Fine-Structure Constant of Freestanding Graphene Measured in Graphite

James P. Reed, *et al.*

Science **330**, 805 (2010);
DOI: 10.1126/science.1190920

The Effective Fine-Structure Constant of Freestanding Graphene Measured in Graphite

James P. Reed,[1] Bruno Uchoa,[1] Young Il Joe,[1] Yu Gan,[1] Diego Casa,[2] Eduardo Fradkin,[1] Peter Abbamonte[1]*

Electrons in graphene behave like Dirac fermions, permitting phenomena from high-energy physics to be studied in a solid-state setting. A key question is whether or not these fermions are critically influenced by Coulomb correlations. We performed inelastic x-ray scattering experiments on crystals of graphite and applied reconstruction algorithms to image the dynamical screening of charge in a freestanding graphene sheet. We found that the polarizability of the Dirac fermions is amplified by excitonic effects, improving screening of interactions between quasiparticles. The strength of interactions is characterized by a scale-dependent, effective fine-structure constant, $\alpha_g^*(\mathbf{k}, \omega)$, the value of which approaches $0.14 \pm 0.092 \sim 1/7$ at low energy and large distances. This value is substantially smaller than the nominal $\alpha_g = 2.2$, suggesting that, on the whole, graphene is more weakly interacting than previously believed.

Graphene is a single layer of carbon atoms with an unusual electronic structure that mimics the massless Dirac equation, allowing phenomena familiar from high-energy physics to be investigated in a solid-state setting (*1*). Because of its low density of states near the Fermi level, it is possible to tune the effective carrier density of graphene with a gate voltage. This makes graphene the potential foundation for a new generation of low-cost, flexible electronics (*1*).

It is widely believed that graphene, if isolated from substrate effects, should be a strongly interacting electron system. (*1*–*8*) The strength of Coulomb interactions in graphene is measured by the ratio of its potential energy to its kinetic energy, $U/K = e^2/\hbar v_F = 2.2$, where e is the charge of an electron, $\hbar$ is Planck's constant, and v_F is the Fermi velocity of the Dirac particles. This ratio is independent of the carrier density and is usually referred to as the fine-structure constant, α_g. Unlike the analogous quantity $\alpha = 1/137$ in quantum electrodynamics (QED), α_g is greater than unity; thus, there is no small expansion parameter for electromagnetic interactions, which have been predicted to lead to novel ground states such as an excitonic insulator (*3*) or a perfect fluid that might exhibit electronic turbulence (*4*).

Surprisingly, so far there is little direct evidence for strong interactions in graphene. The hallmark of interactions is a logarithmically divergent renormalization of the Fermi velocity, v_F (*5*, *8*). However, this effect has not been observed in either angle-resolved photoemission spectroscopy (ARPES) experiments (*9*, *10*) or in scanning single-electron transistor (SET) measurements of the electronic compressibility (*11*). A recent optical infrared measurement observed a departure from the noninteracting spectrum (*12*); however, the effect is not logarithmic and does not agree with ARPES or SET measurements. Interaction effects have been observed in high magnetic fields, but in this case the kinetic energy is quenched by the formation of Landau levels (*13*–*15*). Some of these measurements were done on supported graphene, which can suppress interactions through substrate dielectric screening. However, recent measurements show that freestanding graphene in zero field also behaves like a simple semimetal (*16*).

The absence of a v_F renormalization seems irreconcilable with a large value of the fine-structure constant. However, the particles measured in experiments are not bare electrons, but dressed quasiparticles, which interact via the screened Coulomb interaction (*17*). Hence, a better measure of the strength of interactions is the dressed fine-structure constant, $\alpha_g^*(\mathbf{k}, \omega) = \alpha_g/\varepsilon(\mathbf{k}, \omega) = \alpha_g[1 + V(k)\chi(\mathbf{k}, \omega)]$, where $V(k) = 2\pi e^2/k$ is the bare Coulomb interaction in two dimensions, $\varepsilon(\mathbf{k}, \omega)$ is the dielectric function, and $\chi(\mathbf{k}, \omega)$ is the charge response function of graphene. Unlike α_g, $\alpha_g^*(\mathbf{k}, \omega)$ describes the retarded interaction among the dressed quasiparticles and accounts for the influence of screening generated dynamically within the Dirac system (*18*). $\alpha_g^*(\mathbf{k}, \omega)$ is not a "background" dielectric constant, but a parameter that accounts for the dynamically generated screening by the valence electrons. Diagrammatic calculations may be structured in powers of $\alpha_g^*(\mathbf{k}, \omega)$, so this function can be considered a valid expansion parameter (*19*).

To determine $\alpha_g^*(\mathbf{k}, \omega)$, one must determine the response function, $\chi(\mathbf{k}, \omega)$, which is a general representation of the charge dynamics of the system. In real space, $\chi(\mathbf{r}_1 - \mathbf{r}_2, t)$ represents the amplitude that a disturbance in the electron density at $\mathbf{r}_1$ will propagate to $\mathbf{r}_2$ after an elapsed time, t. $\chi(\mathbf{k}, \omega)$ also describes, in linear response theory, how the system responds to charged perturbations via

$$n_{ind}(\mathbf{k}, \omega) = V(\mathbf{k})\ \chi(\mathbf{k}, \omega)\ n_{ext}(\mathbf{k}, \omega) \qquad (1)$$

where $n_{ext}(\mathbf{k}, \omega)$ is an arbitrary source and $n_{ind}(\mathbf{k}, \omega)$ is the charge induced in the medium (*20*).

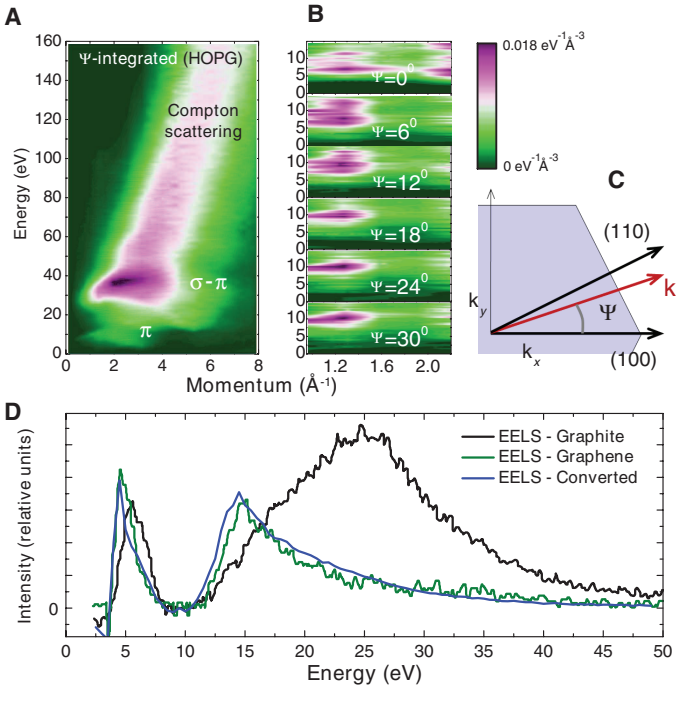

Fig. 1. IXS experiments from graphite and extraction of the response function for graphene. (**A**) Scattered intensity as a function of energy and momentum for highly oriented pyrolitic graphite (HOPG), which gives the Ψ-integrated response. (**B**) Angle-resolved spectra from single-crystal graphite for the domain over which anisotropy was observed. (**C**) Brillouin zone of graphene with various vectors defined. (**D**) Test of Eq. 4 on the electron energy loss experiments of Eberlein (*24*) (fit value $k = 0.33$ Å^{-1}), showing that an accurate response for graphene can be obtained from IXS experiments on graphite.

[1]Department of Physics and Frederick Seitz Materials Research Laboratory, University of Illinois, Urbana, IL 61801, USA. [2]Advanced Photon Source, Argonne National Laboratory, 9700 South Cass Avenue, Argonne, IL 60439, USA.

*To whom correspondence should be addressed. E-mail: abbamonte@mrl.uiuc.edu

To determine $\chi(\mathbf{k}, \omega)$ for graphene, we performed inelastic x-ray scattering (IXS) experiments on single crystals of graphite, which consists of layers of graphene loosely bound by electrostatic van der Waals forces. IXS measures the dynamic structure factor, $S(\mathbf{k}, \omega)$, which is related to the imaginary part of the charge response through the quantum mechanical version of the fluctuation-dissipation theorem (*20*, *21*)

$$S(\mathbf{k}, \omega) = -\frac{1}{\pi}\frac{1}{1 - e^{-\hbar\omega/kT}}\mathrm{Im}[\chi_{3D}(\mathbf{k}, -\mathbf{k}, \omega)] \quad (2)$$

where T is the temperature and χ_{3D} is the charge response of graphite. Equation 2 provides only the imaginary part of χ_{3D}; if a sufficiently broad energy spectrum is sampled in the experiment, the real part may be determined by the Kramers-Kronig (KK) transform (*21*, *19*). We note that, because graphite is layered, its electron density is nonuniform, so $\chi_{3D} = \chi_{3D}(\mathbf{k}, \mathbf{G} - \mathbf{k}, \omega)$ is a function of two momenta, $\mathbf{G}$ being a reciprocal lattice vector. IXS experiments provide the $\mathbf{G} = 0$ component (*21*, *19*).

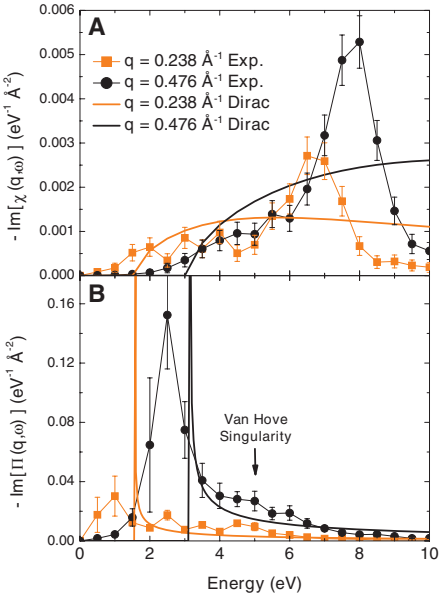

Fig. 2. Response functions for graphene in the low-momentum region, showing the Dirac particles. (**A**) $-\mathrm{Im}[\chi(\mathbf{k}, \omega)]$. The Dirac spectrum is visible as a continuum below the π plasmon, which arises from the Van Hove singularity at the top of the π band. Also shown is the expected response for idealized, noninteracting Dirac fermions, using Eq. 3 and $\Pi(\mathbf{k}, \omega) = -k^2/\left(4\sqrt{(\hbar v_F q)^2 - \omega^2}\right)$, with $v_F = 10^6$ m/s. The curves are plotted on an absolute scale, and the magnitudes may be directly compared. (**B**) Experimental and idealized $-\mathrm{Im}[\Pi(\mathbf{k}, \omega)]$, showing the locations of single-particle excitations. The peak in the measured response is 0.6 eV lower in energy than the ideal response, indicating excitonic effects, which transfer spectral weight from the Van Hove singularity to the Dirac spectrum.

The IXS spectra, shown in Fig. 1, A and B (*19*), are dominated by two collective excitations, at approximately 6 eV and 35 eV, which were observed in previous studies (*22*, *23*) and are normally referred to as the π and σ–π plasmons, respectively. These excitations are, however, not plasmons in the usual sense; they do not arise from free carrier screening but from Van Hove singularities in the band structure. The former resides at the edge of the π bands near the M point in the Brillouin zone, and the latter in the σ-bonded bands along the A-L line (*23*). Beneath the plasmons, a continuum of single-particle excitations is visible. The spectra were measured, for $k_z = 0$, throughout an entire, symmetry-independent sector of the Brillouin zone (Fig. 1C).

Although these experiments were done on graphite crystals, the results are directly relevant to graphene. Graphite is a quasi-two-dimensional system in which the interlayer hopping, $t_\perp = 0.4$ eV, is much smaller than that in-plane, $t_\parallel = 3$ eV. At energy scales greater than $t_\perp$, the π band of graphite is essentially the same as in graphene, and the system can be thought of as a stack of graphene sheets coupled only by direct, long-ranged Coulomb interactions.

More quantitatively, graphite and graphene have approximately the same polarizability, $\Pi(\mathbf{k}, \omega)$. Physically, Π can be thought of as the response of the system, excluding direct Coulomb interactions, which couple the layers, and is related to the response function by

$$\chi(\mathbf{k}, \omega) = \frac{\Pi(\mathbf{k}, \omega)}{1 - V(\mathbf{k})\Pi(\mathbf{k}, \omega)} \quad (3)$$

Making the assumption that Π is the same for both graphite and graphene, and that the graphene sheets are very thin, we acquire an expression (*19*) for the response of graphene in terms of that for graphite

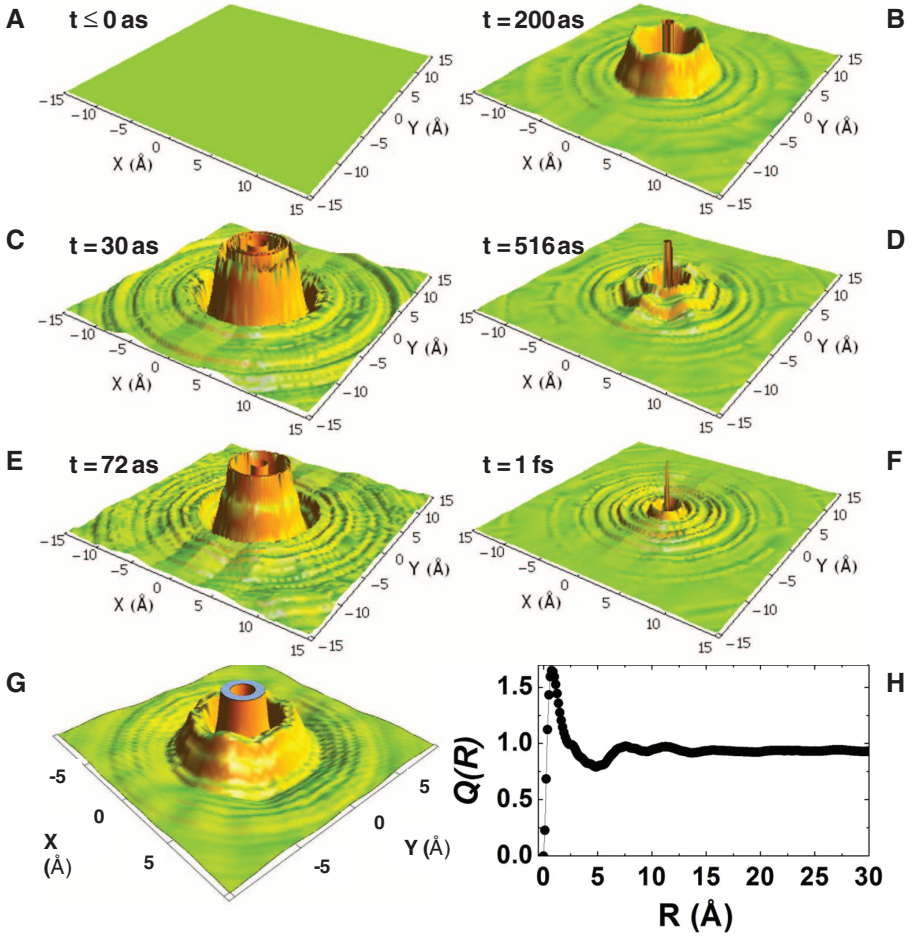

Fig. 3. Dynamics of the valence electrons in graphene. (**A** to **F**) Dynamical electron density, $n_{ind}(x, y, t)$, induced by a point source appearing at the origin and then instantaneously disappearing. We have taken $e = 1$. Densities are plotted over a field of view of 30 Å by 30 Å at selected times. The vertical scale has been truncated at ±5.0 Å^{-2} as^{-1} to magnify the finer features. The resolutions for these images were $\Delta\mathbf{r} = 0.20$ Å and $\Delta t = 10.3$ as. The time resolution is fast in comparison with currently available laser pulses. (**G**) Time-independent electron density, $n_{ind}(x, y)$, induced by a static point charge. The vertical scale has been truncated at ±0.04 Å^{-2} to magnify the finer features. (**H**) Integrated density $Q(R)$, giving an asymptotic value of $Q(\infty) = (0.924 \pm 0.046)e$, showing that a static point charge in graphene is screened nearly completely.

$$\chi(\mathbf{k},\omega)=\frac{\chi_{3D}(\mathbf{k},-\mathbf{k},\omega)\cdot d}{1-V(\mathbf{k})[1-F(\mathbf{k})]\chi_{3D}(\mathbf{k},-\mathbf{k},\omega)\cdot d} \quad (4)$$

where d = 3.35 Å is the distance between the layers and

$$F(\mathbf{k})=\frac{\sinh(qd)}{\cosh(qd)-\cos(k_z d)} \quad (5)$$

is a form factor that describes the layered structure of graphite, q and k_z being the magnitude of the in- and out-of-plane components of $\mathbf{k}$, respectively (*19*). Equation 4 can be thought of as a means of turning off the Coulomb interaction between the layers, revealing the response for half-filled, freestanding graphene.

To test Eq. 4, we applied it to an electron energy loss (EELS) study by Eberlein (*24*) of the dielectric loss function $-\mathrm{Im}[1/\varepsilon(\mathbf{k},\omega)]$, which is proportional to $\mathrm{Im}[\chi]$, for both graphite and freestanding graphene. They found that the π and σ–π plasmons are also present in graphene but are shifted to lower energy compared with graphite because of the reduced dimensionality (*23*, *24*). We scaled their graphite spectra with the f-sum rule, KK transformed, applied our Eq. 4, and compared the results to their spectra for graphene (Fig. 1D). The curves match nearly exactly, reproducing the red shifts and changes in spectral weight of the two plasmons. We conclude that Eq. 4 provides a valid response function for freestanding graphene at energy scales greater than $t_\perp$ (*19*).

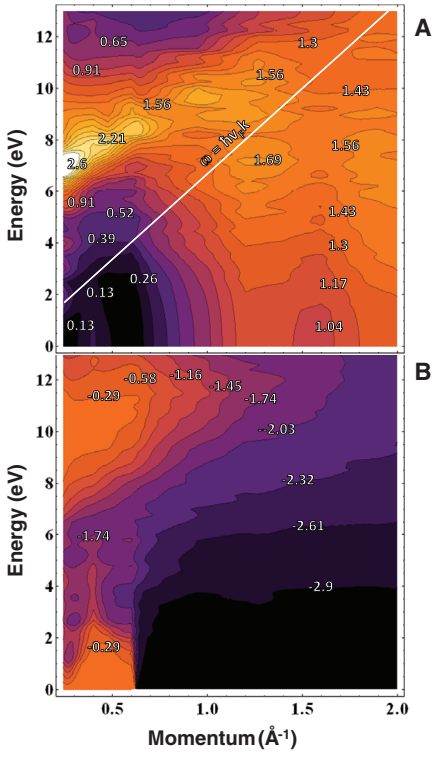

Fig. 4. The effective, screened fine-structure constant, $\alpha_g^*(\mathbf{k},\omega)$, as defined in the text. (**A**) The magnitude of $\alpha_g^*(\mathbf{k},\omega)$, plotted against momentum and energy. The Dirac dispersion $\omega=\hbar v_F k$ is indicated by the white line. In the low momentum region, $\alpha_g^*(\mathbf{k},\omega)$ is larger above this line than below. (**B**) The phase of $\alpha_g^*(\mathbf{k},\omega)$, in radians.

At the lowest momenta measured, the $\chi(\mathbf{k},\omega)$ derived from Eq. 4 shows signatures of the Dirac fermions. In Fig. 2A, we plot $-\mathrm{Im}[\chi(\mathbf{k},\omega)]$ as a function of ω for two momenta at which the quantity $\hbar v_F k$ is less than the energy of the Van Hove singularity in the π band. Also shown is the spectrum for idealized, noninteracting Dirac fermions. A continuum is visible below 5 eV whose magnitude and dispersion with $\mathbf{k}$ are close to that expected for Dirac particles. This suggests that the low-frequency, long-wavelength response of graphene is strongly influenced by the Dirac fermions. The experimental and idealized spectra differ, however, in two respects. First, the curves deviate near the energy of the π plasmon, because in the real material the width of the π band is finite. Second, the experimental onset energy is lower and smoother than expected.

The origin of these discrepancies is clarified by examining the polarization function, $-\mathrm{Im}[\Pi(\mathbf{k},\omega)]$, shown in Fig. 2B, which exhibits peaks at the energy of single-particle transitions rather than of the collective modes. Again, the curves for idealized Dirac fermions are shown. The peak in the data is broader and shifted to lower energy, by approximately 0.6 eV, compared with the idealized spectrum. Further, the spectral weight in the Van Hove singularity is suppressed from what is expected (*23*), being reduced to a shoulder on the Dirac spectrum. These effects may be understood as arising from a combination of band curvature (i.e., deviation from the Dirac spectrum at high energy), as well as excitonic effects, which are known to transfer spectral weight to lower energy in particle-hole spectra. We note that the 0.6-eV shift is similar in magnitude to that predicted by recent ab initio calculations employing the Bethe-Saltpeter equation (*25*, *26*).

To observe how excitations in graphene propagate in real time, in Fig. 3, A to F, we plot the time-dependent charge density, $n_{ind}(\mathbf{r},t)$, arising from a point source in graphene, determined by using $n_{ext}(\mathbf{k},\omega)=-e$ in Eq. 1. As expected from causality, $n_{ind}=0$ for $t<0$. The earliest response ($t<200$ as) is dominated by the fast, broadband, σ–π plasmon, which is isotropic and ~5 Å in size because of the localized character of the sp^2 bonds. The narrower π plasmon emerges later ($t>200$ as), extends over ~10 Å, and exhibits six-fold rotational symmetry. One can think of the sequence of events as a localized burst of density that back-scatters off the atomic lattice.

The effective fine-structure constant, $\alpha_g^*(\mathbf{k},\omega)$, is shown in Fig. 4. $\alpha_g^*(\mathbf{k},\omega)$ is a valid coupling constant at low energy where the bands are Dirac-like; at high energy, it may be thought of simply as the inverse dielectric function, scaled by α_g. Figure 4 shows that α_g^* is complex, and is not a constant but is a strong function of frequency and momentum. This indicates that the strength of interactions in graphene depends on the scale on which the system is probed. The magnitude of α_g^* ranges from greater than 2 at high energy to much less than unity at energies lying below the $\omega=\hbar v_F k$ line (Fig. 4).

An important limit is that of zero frequency and small momentum. At the lowest momenta measured, we found that $\Pi(\mathbf{k},0)\sim k$ as $k\to 0$ (*19*). Extrapolating linearly to zero, we find that $\alpha_g^*(0^+,0)\equiv\lim_{\mathbf{k}\to 0}\alpha_g^*(\mathbf{k},0)=0.14\pm0.092\approx 1/7$, which may be thought of as a static dielectric constant of $\varepsilon=[1-Q(\infty)/e]^{-1}=15.4^{+39.56}_{-6.45}$ (*19*). This large value, which is an outcome of the excitonic shifts shown in Fig. 2B, is 3.5 times as large as past estimates based on the random phase approximation (RPA) (*27*) or GW methods (*26*) in which excitonic effects were neglected. The small value of α_g^* in this limit indicates that graphene can screen very effectively over finite distances and should act like a weakly interacting system for phenomena that take place at low energy and modest wave vector.

For illustration, we simulate the response of the system to a charged impurity by solving Eq. 1 with $n_{ext}(\mathbf{k},0)=-e$. The induced charge $n_{ind}(\mathbf{r})$ (Fig. 3G) is a cloud ~10 Å in size, comprising an isotropic inner layer surrounded by a six-fold symmetric outer layer, reminiscent of the excitations in Fig. 3, A to F. Figure 3H shows $Q(R)$, which is the total charge contained in $n_{ind}(\mathbf{r})$ within a shell of radius R. $Q(R)$ oscillates and plateaus at large R to the value $Q(\infty)=(0.924\pm0.046)e$. Hence, at length scales larger than a few nanometers, a charged impurity in graphene is screened nearly completely. This explains the surprisingly small sensitivity of the mobility of graphene to a high-κ dielectric environment (*28*, *29*), which was anticipated to reduce scattering from charged impurities. Because graphene already screens impurities very efficiently, immersing it in a high-κ environment does not substantially influence its properties. Screening effects may also explain the absence of a detectable velocity renormalization in recent ARPES and SET experiments. Overall, our results indicate that graphene is a more weakly interacting system than previously assumed and that the mobility of graphene may currently be limited by some phenomenon other than scattering from charged impurities.

References and Notes

1. A. H. Castro Neto, F. Guinea, N. M. R. Peres, K. S. Novoselov, A. K. Geim, *Rev. Mod. Phys.* **81**, 109 (2009).
2. K. S. Novoselov *et al.*, *Science* **306**, 666 (2004).
3. J. E. Drut, T. A. Lähde, *Phys. Rev. Lett.* **102**, 026802 (2009).
4. M. Müller, J. Schmalian, L. Fritz, *Phys. Rev. Lett.* **103**, 025301 (2009).
5. J. González, F. Guinea, M. A. H. Vozmediano, *Nucl. Phys. B* **424**, 595 (1994).
6. D. E. Sheehy, J. Schmalian, *Phys. Rev. Lett.* **99**, 226803 (2007).

7. Y. Barlas, T. Pereg-Barnea, M. Polini, R. Asgari, A. H. MacDonald, *Phys. Rev. Lett.* **98**, 236601 (2007).
8. E. H. Hwang, B. Y.-K. Hu, S. Das Sarma, *Phys. Rev. Lett.* **99**, 226801 (2007).
9. S. Y. Zhou *et al.*, *Nat. Phys.* **2**, 595 (2006).
10. A. Bostwick, T. Ohta, T. Seyller, K. Horn, E. Rotenberg, *Nat. Phys.* **3**, 36 (2007).
11. J. Martin *et al.*, *Nat. Phys.* **4**, 144 (2008).
12. Z. Q. Li *et al.*, *Nat. Phys.* **4**, 532 (2008).
13. K. I. Bolotin, F. Ghahari, M. D. Shulman, H. L. Stormer, P. Kim, *Nature* **462**, 196 (2009).
14. X. Du, I. Skachko, F. Duerr, A. Luican, E. Y. Andrei, *Nature* **462**, 192 (2009).
15. J. C. Checkelsky, L. Li, N. P. Ong, *Phys. Rev. B* **79**, 115434 (2009).
16. X. Du, I. Skachko, A. Barker, E. Y. Andrei, *Nat. Nanotechnol.* **3**, 491 (2008).
17. D. Pines, P. Nozières, *The Theory of Quantum Liquids* (Perseus Books, Cambridge, MA, 1999).
18. F. Aryasetiawan, O. Gunnarsson, *Rep. Prog. Phys.* **61**, 237 (1998).
19. Materials and methods are available as supporting material on Science Online.
20. W. Schülke, *Electron Dynamics by Inelastic X-Ray Scattering* (Oxford Univ. Press, Oxford, 2007).
21. P. Abbamonte *et al.*, *Adv. Mater.* **22**, 1141 (2010).
22. N. Hiraoka, H. Ishii, I. Jarrige, Y. Q. Cai, *Phys. Rev. B* **72**, 75103 (2005).
23. A. G. Marinopoulos, L. Reining, A. Rubio, V. Olevano, *Phys. Rev. B* **69**, 245419 (2004).
24. T. Eberlein *et al.*, *Phys. Rev. B* **77**, 233406 (2008).
25. L. Yang, J. Deslippe, C.-H. Park, M. L. Cohen, S. G. Louie, *Phys. Rev. Lett.* **103**, 186802 (2009).
26. P. E. Trevisanutto, M. Holzmann, M. Côté, V. Olevano, *Phys. Rev. B* **81**, 121405 (2010).
27. M. Polini, A. Tomadin, R. Asgari, A. H. MacDonald, *Phys. Rev. B* **78**, 115426 (2008).
28. L. A. Ponomarenko *et al.*, *Phys. Rev. Lett.* **102**, 206603 (2009).
29. C. Jang *et al.*, *Phys. Rev. Lett.* **101**, 146805 (2008).

30. We gratefully acknowledge helpful discussions with A. H. MacDonald, D. Maslov, P. Guinea, L. Levitov, and A. J. Millis, and Y. Cai for supplying graphite crystals. This work was supported by the U.S. Department of Energy under grants DE-FG02-07ER46459 and DE-FG02-07ER46453 through the Frederick Seitz Materials Research Laboratory, with use of the Advanced Photon Source supported by DEAC02-06CH11357.

Supporting Online Material

www.sciencemag.org/cgi/content/full/330/6005/805/DC1
Materials and Methods
SOM Text
Figs. S1 to S6
References
Movies S1 and S2

14 April 2010; accepted 27 September 2010
10.1126/science.1190920

Large-Area Three-Dimensional Molecular Ordering of a Polymer Brush by One-Step Processing

Nobuhiko Hosono,[1,2] Takashi Kajitani,[2] Takanori Fukushima,[2]* Kazuki Ito,[3] Sono Sasaki,[4] Masaki Takata,[3,4] Takuzo Aida[1,2]*

Rational molecular design and processing, enabling large-area molecular ordering, are important for creating high-performance organic materials and devices. We show that, upon one-step hot-pressing with uniaxially stretched Teflon sheets, a polymer brush carrying azobenzene-containing mesogenic side chains self-assembles into a freestanding film, where the polymer backbone aligns homeotropically to the film plane and the side chains align horizontally. Such an ordered structure forms through translation of a one-dimensional molecular order of the Teflon sheet and propagates from the interface macroscopically on both sides of the film. The resultant wide-area bimorph configuration allows the polymer film to bend rapidly and reversibly when the azobenzene units are photoisomerized. The combination of polymer brushes with hot-pressing and Teflon sheets provides many possibilities in designing functional soft materials.

In biological systems, long-range three-dimensional (3D) molecular ordering, realized by programmed spontaneous assembly of dedicated functional molecules, is crucial to the activities of living organisms. This notion has inspired chemists to develop methods for tailoring elaborate molecular assemblies over a macroscopic length scale, because they are considered promising for creating cutting-edge organic materials and devices (*1*–*3*). Examples include shear forces, external fields, and patterned surfaces, which allow 1D macroscopic ordering of certain polymers and liquid crystalline molecules (*4*–*10*). However, neither rational molecular design strategy nor processing methodology has yet been developed for 3D ordering of large and/or complex molecules in macroscopic solid materials. We report a serendipitous discovery that hot-pressing of a certain polymer brush, sandwiched by uniaxially stretched Teflon sheets, affords a freestanding film, in which a 3D molecular order with a remarkably high structural integrity develops widely in a macroscopic length scale (Fig. 1). The width of the film, fabricated by this easy processing, is in principle unlimited.

The polymer brush consists of a polymethacrylate backbone densely grafted to paraffinic side chains containing three azobenzene units that then wrap around the backbone (poly-**1**, Fig. 1B). Due to a size-exclusion effect, grafted side chains tend to be expelled from the polymer backbone, whereas the backbone itself is likely extended (*11*–*13*). Consequently, the polymer brush adopts a cylindrical shape (Fig. 1C). Azobenzene is a frequently used photochromic motif, which undergoes molecular deformations associated with its trans-to-cis and reverse isomerizations upon irradiation with ultraviolet (UV) and visible light, respectively (*14*–*16*). As exemplified by the pioneering work of Ikeda and coworkers (*17*, *18*), incorporation of azobenzene units into cross-linked polymer networks affords liquid crystalline elastomers capable of photoactuation. In all successful examples (*17*–*21*), the photomechanical effect relies on a phase transition between liquid crystal and isotropic phases triggered by the azobenzene isomerization. Our interest in the present work was to explore the possibility that polymer brushes, which can accommodate multiple azobenzene units in their densely packed side chains, might show a photomechanical response even without cross-linking. However, a freestanding cast film of poly-**1** did not respond to light irradiation. We wondered whether this result might be due to a roughness of the cast film. So, the cast film was sandwiched by Teflon sheets and hot-pressed. The resulting film underwent a reversible bending motion upon alternate irradiation with UV and visible lights. We also noticed that this photomechanical response hardly emerges when the Teflon sheets are arranged in such a way that their drawing directions are orthogonal to one another.

Poly-**1** was obtained by free-radical polymerization of **1** (Fig. 1A and fig. S1) (*22*). In differential scanning calorimetry (DSC), poly-**1** showed, on cooling from its isotropic melt, two exothermic peaks at 120° and 103°C (fig. S2), indicating the presence of a mesophase. Synchrotron radiation small-angle x-ray scattering (SAXS) of a bulk sample of poly-**1**, prepared by heating to its hot melt followed by cooling to the mesophase temperature in a glass capillary (*22*), displayed clear reflection peaks (Fig. 2A) assignable to a 2D rectangular lattice (space group; $P2_1/a$, Fig. 2B) with lattice parameters a and b of 218(5) and 147(1) Å, respectively. Judging from the magnitudes of a and b, the cylinders of poly-**1** most likely deform elliptically to some extent and align parallel to one another without entanglement of their side chains. The SAXS pattern hardly changed when the sample was allowed to solidify by cooling down to room temperature (fig. S3A). Meanwhile, in a wide-angle region (fig. S3B), a broad peak with a d-spacing of 4.4 Å split into two (5.0 and 4.3 Å) upon solidification of the material, suggesting that the azobenzene-containing paraffinic side chains of poly-**1** are structured.

When poly-**1** was thermally treated by hot-pressing with stretched Teflon sheets, a film

[1]Department of Chemistry and Biotechnology, School of Engineering, The University of Tokyo, 7-3-1 Hongo, Bunkyo, Tokyo 113-8656, Japan. [2]RIKEN Advanced Science Institute, 2-1 Hirosawa, Wako, Saitama 351-0198, Japan. [3]RIKEN SPring-8 Center, 1-1-1 Kouto, Sayo, Hyogo 679-5198, Japan. [4]Japan Synchrotron Radiation Research Institute (JASRI), 1-1-1 Kouto, Sayo, Hyogo 679-5198, Japan.

*To whom correspondence should be addressed. E-mail: fukushima@riken.jp (T.F.); aida@macro.t.u-tokyo.ac.jp (T.A.)